HEFAT2008
6th International Conference on Heat Transfer, Fluid Mechanics and Thermodynamics
30 June to 2 July 2008
Pretoria, South Africa
Paper number: MG1

Secondary Flows and Upstream Film Cooling in a Linear NGV Cascade in Compressible Flows: Computations and Experiments

Gazi I. Mahmood*
Mechanical & Aeronautical Engineering Department, University of Pretoria, South Africa
Arun K. Saha
Mechanical Engineering Department, Indian Institute of Technology at Kanpur, India
Sumanta Acharya
Turbine Innovative Energy Research (TIER) Center, Louisiana State University, USA
*Corresponding author, E-mail: gazi.mahmood@up.ac.za

Abstract

The secondary flows along the endwall of a high speed two-dimensional passage employing the GE-E^3 nozzle guide vane (NGV) airfoil are presented from computational simulations. Then the adiabatic film-cooling effectiveness with the cooling holes located upstream of the two-dimensional vane cascade employing the same GE-E^3 airfoil is measured and presented. The cascade inlet velocity is 114.6 m/s and exit Mach number is 1.05, while the experimental conditions employ an inlet velocity of 60 m/s and exit Mach number of about 1.0. The objectives of the research are to investigate the effects of the near endwall secondary flows on the endwall heat transfer and film-cooling effectiveness in the passage with the compressible flows. The computational results show the high temperature regions on the endwall near the leading edge region and pressure side. The results from the measurements indicate film cooling effectiveness is very small on a large endwall region near the pressure side for the blowing ratio (M_{in}) below 2.0. This occurs as the secondary vortex structures prevent the film cooling jets to penetrate into the pressure-side regions. However, the cooling effectiveness is higher near the passage suction side for all the blowing ratios tested.

Nomenclature

C, C_{ax} = actual and axial chord, respectively, of vane airfoil
M_{in} = inlet blowing ratio of film-cooling flow
Nu = Nusselt number on passage bottom endwall
P, S = pitch and span, respectively, of vane passage
PS, SS, SP = pressure side, suction side, and stagnation line, respectively, of vane passage
P_d = dynamic pressure based on passage inlet conditions
P_e = exit pressure (static) from passage
P_o, U_o, T_o = reference pressure (static), velocity, and temperature (static) at passage inlet, respectively
S_x = normal distance from vane surface
T_b, T_w = temperature on vane surface and endwall, respectively
(X_G, Y_G, Z_G) = right hand Cartesian global coordinates
(X, Y, Z) = local coordinates from vane pressure side
Ω_s = vorticity along local streamwise direction
Ω_n, Ω_z = vorticities normal to analysis plane
τ_z = wall shear stress along axial direction, Z_G
ε = adiabatic film-cooling effectiveness

Introduction

The vortical structure of secondary flows near endwall in a turbine nozzle guide vane (NGV) passage enhance fluid transport between the wall boundary layer and hot gas streak in the mean flow. The secondary flows thus increase thermal load on the endwall and lift up the film-cooling flow injected to provide protective cover on the endwall. The coolant effectiveness is thus severely reduced and the heat transfer to endwall increases along the development regions of the secondary flows. The present investigation is aimed to computationally determine the development of the secondary flows near the endwall and then explain the behavior of the measured film cooling effectiveness along the endwall in a linear vane passage.

The development of the secondary flow structures in linear vane passages is illustrated by Kang and Thole [1], Radomsky and Thole [2], Hermanson et al. [3], and Dominy and Harding [4] from numerical simulations as well as measurements in the cascades. The flow field in the vane passage is incompressible in all the studies. The studies reveal that the secondary vortex flow is initiated near the junction of leading edge and endwall. This is termed as the horseshoe vortex. The horseshoe vortex is then advected along the vane pressure side and suction side as the pressure side leg and suction side leg vortex, respectively. As the pressure side leg vortex is driven toward the passage suction side by the cross-flow, it grows in strength and size by the endwall boundary layer fluid and passage pressure gradient and becomes the passage vortex. Near the suction side, the passage vortex groups with the suction side leg vortex to form the passage vortex system which lifts up from the endwall region, but continues to grow as it moves along the vane suction side toward the passage exit.

The effects of cooling hole and slot bleed configurations upstream of linear vane passages on the film-cooling effectiveness are described in details by the investigators in [6-

10]. The configurations include single and multiple rows of cylindrical or fan-shaped holes, slots of different area ratios, and partially blocked slots. The results indicate the slot-bleed cooling is better compared to the discrete hole cooling in terms of both the adiabatic effectiveness and aerodynamics to reduce the secondary vortices, but at the expense of high coolant mass flux. The investigations employ incompressible flow and do not explicitly reveal the roles of the near wall secondary flows on the behavior of film coverage.

The present numerical study in a linear vane passage determines the locations, size, and strength of the secondary vortices along the endwall and indicates their roles on the endwall thermal load. The experimental investigation then shows their adverse effects on the coolant jet trajectories and film coverage. The flow field employed is compressible in both the numerical and experimental investigations. The results are expected to provide the turbine designers with guidelines for better cooling hole configurations.

Computational model

The computations are performed in a two-dimensional vane passage employing the airfoil section of GE-E^3 first stage vane at the hub-side. The passage is 4.7 times of the original first stage geometry. Table 1 shows the geometry of the numerical domain.

Table 1: Geometry of Computations

Scale factor	*C (m)*	C_{ax} *(m)*	*C/S*	*C/P*
4.7X	0.28	0.16	1.48	1.33

Figure 1(b) shows the computational domain that uses one vane with periodic boundary in the pitchwise direction over one pitch of the passage. In the axial direction, the inlet and outlet are located $1.93C_{ax}$ and $2.42C_{ax}$ from the vane leading edge. The inlet and exit boundary conditions are set at these locations, respectively. The velocity and temperature profiles at the inlet are set uniform. Air is chosen as the working fluid. The inlet flow angle is zero degree same as the design condition. Table 2 provides the boundary conditions employed for the computations.

Table 2: Boundary Conditions for Computations

U_o *(m/s)*	P_o *(Pa,g)*	P_o/P_e	T_o *(K)*	T_w, T_b *(K)*	*wall*
114.6	1.07E+05	2.06	1200	923	No-slip

Calculations are performed with the solver FLUENT after generating grids in the GRIDPRO. The number of grid points used is 1.2 million with near-wall stretching of the grid points toward the bottom endwall. Realizable k-ε with two-layer near wall turbulent model is employed to simulate the flow. All the flow variables presented here are converged to residual levels of order of 10^{-4} while the residual level for the temperature field is 10^{-7}. The full domain in the spanwise direction is computed with the no-slip boundary condition at the top and bottom walls.

Experimental test facility

The measurements are obtained in a high speed cascade facility employing one full vane profile and two one-half profiles of the vane airfoil as shown in Fig. 1(a). The two-dimensional vanes in the test section employs the same GE-E^3 vane airfoils as in the computations, but the test section geometry uses 1X scale of the actual guide vane passage geometry as indicated in Table 3. The inlet flow angle is zero degree as in the computations. Surface pressure tap holes at the vane mid-span are connected to the cylindrical holes located slightly beneath the vane profile. These holes are then connected via rubber tubings through a top wall window to a DSA 16 channel high speed pressure scanner.

Table 3: Geometry of Cascade Test Section

Scale factor	*C (m)*	C_{ax} *(m)*	*C/S*	*C/P*
1X	0.06	0.034	1.48	1.33

Nine copper-constantan thermocouples are located in the bottom endwall of the measurement passage (Fig. 1a). The wall is covered with thin Kapton tape and the thermocouple tips are located just beneath the tape to measure the adiabatic surface temperature. Compressed air enters the test section with Mach number 0.20, static pressure 81.1 *kPa* (gage), and static temperature 295 *K*. The inlet-to-exit static pressure ratio is 1.80 and the exit Mach number is about 1.0 choking the flow at the passage throat. Two tailboards pivoted at the trailing edge can be swung to adjust the mass flow in the two passages in the test section and provide a periodic condition.

Two rows of cylindrical film cooling holes are located $0.20C_{ax}$ upstream of the cascade passage as shown in Fig. 1(a). The distance between the 1st and 2nd row of holes is $0.07C_{ax}$. Each hole is oriented at 30^o relative to the endwall surface and has a length-to-diameter ratio of 7.90. The jet angle from the first row is parallel to the vane axial direction, while it is 90^o to the vane axial direction from the 2nd row. Compressed air is cooled to a temperature of -7.5 ^oC when it is supplied to a plenum box located under the test section to provide a coolant-to-mainstream temperature ratio of about 0.90. The coordinate system employed for the measurements and computations are also shown in Fig. 1. The maximum uncertainties based on 95% confidence level in the thermocouple temperature and adiabatic-film cooling effectiveness measurements are 0.75% and 6.9%, respectively.

Results and discussions

(i) Computations: flow field and heat transfer

The numerical results are presented in six planes and along the bottom endwall as shown in the table of Fig. 1(b). The planes 1, 2, and 3 are about perpendicular to the local vane surface, while the planes 4, 5, and 6 extend in the pitchwise direction in the passage. The results include distributions of vorticities normal to the analysis planes, vorticity in the local streamwise direction, overall turbulence intensity, endwall wall shear stress and streamlines, and Nusselt numbers along endwall. Such distributions are shown near the endwall region only to identify the secondary flow structures.

Figure 2 shows normalized vorticities ($\Omega_n * C/U_o$) normal to planes 1, 2, and 3. Plane-1 is located at the leading edge, and planes 2 and 3 are located near the leading edge on the pressure and suction side, respectively. The positive vorticity is directed out of the plane as S_x is the distance from the vane surface. The circular contour region of $\Omega_n * C/U_o > 20$ near the stagnation location *SP* indicates the roll-up of horseshoe vortex. As the horseshoe vortex is advected with the boundary flow on two sides of the vane, the vorticities identified in plane 2 and 3 in Fig. 2 indicate the pressure side leg vortex and suction side leg vortex, respectively. The vorticity is negative in the suction side leg vortex region in plane-3 as the direction of vortex rotation is opposite to that of the pressure side leg vortex. As the vortex structures are three-dimensional inside the passage, the vorticities

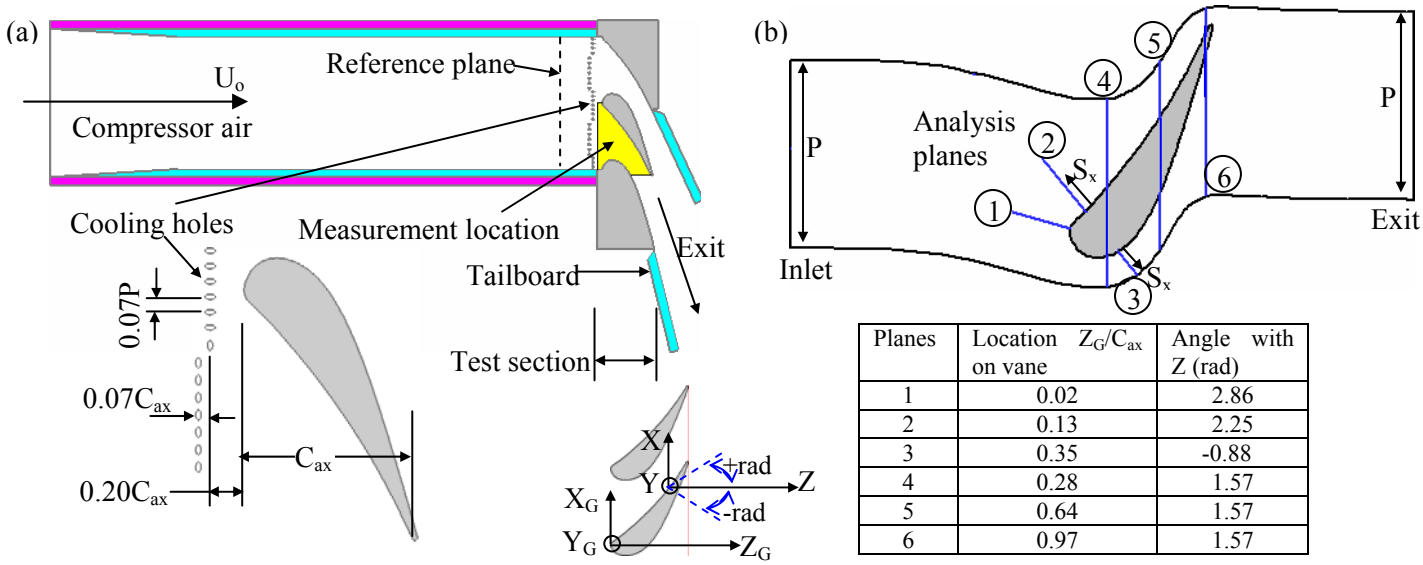

Planes	Location Z_G/C_{ax} on vane	Angle with Z (rad)
1	0.02	2.86
2	0.13	2.25
3	0.35	-0.88
4	0.28	1.57
5	0.64	1.57
6	0.97	1.57

Figure 1: (a) Experimental test set-up showing the vane profile and location of film cooling holes, and (b) Computational domain with flow analysis planes and coordinate systems.

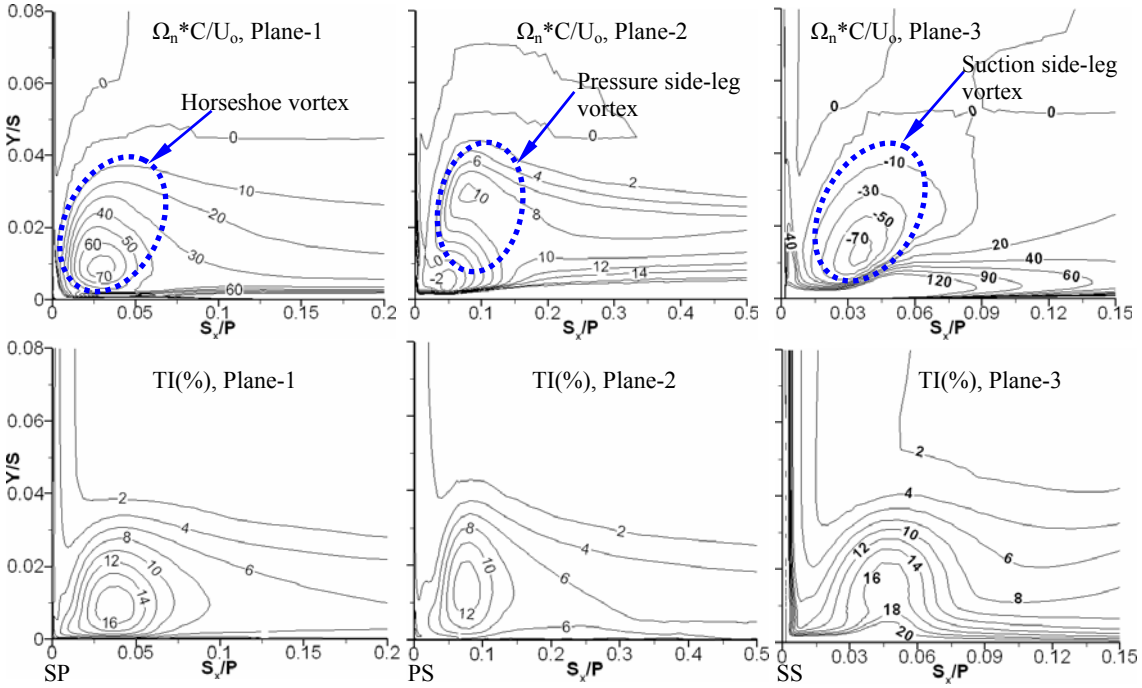

Figure 2: Computational normalized vorticity (Ω_n*C/U_o) normal to Planes-1, 2, and 3 and overall turbulence intensity (*TI%*) in Planes-1, 2, and 3.

in plane 2 and 3 in Fig. 2 do not necessarily indicate the actual size and strength of the pressure and suction side leg vortex, respectively. Figure 2 also presents the overall turbulence intensities (*TI*%) in planes 1, 2, and 3. The high *TI%* magnitudes are located in the vortex regions in these planes. The center locations of high *TI%* contours are at about the same locations as those of the Ω_n*C/U_o contours.

The normalized vorticities and *TI%* in Fig. 3 are presented in the Z_G/C_{ax}=0.28 plane (plane-4) located upstream of the passage throat. The positive (Ω_z*C/U_o)>10 contours near the pressure side (*PS*) indicate the passage vortex structure in this plane, while the negative (Ω_z*C/U_o)<-5 contours near the suction side (*SS*) indicate the suction side leg vortex. The pressure side leg vortex becomes the passage vortex as it moves away from the pressure side inside the vane passage. The two distinct circular (Ω_s*C/U_o) and *TI%* contour regions in Fig. 2 also indicate the passage vortex and suction side leg vortex in the same locations as those given by the (Ω_z*C/U_o) contours. The contour lines with high magnitudes just above and parallel to the endwall (*Y/S*=0.0) are caused by the boundary layer flow.

Figure 4 shows the locations of the vortex structures further downstream in plane-5 at Z_G/C_{ax}=0.64. The circular contour regions of (Ω_z*C/U_o) and (Ω_s*C/U_o) vorticities, and *TI%* between 0.10<*X/P*<0.30 indicate the passage vortex. The high magnitude contour regions between 0.45<*X/P*<0.55 near the suction side indicate the suction-side leg vortex. Note that the (Ω_z*C/U_o) vorticities are negative for the suction side leg vortex as the vortex rotation is opposite to that of the passage vortex. The distance between the two vortex centers is closer in plane-5 than it is in plane-4. The high positive (Ω_z*C/U_o) magnitudes adjacent to the suction side indicate the presence of corner vortex in the flow.

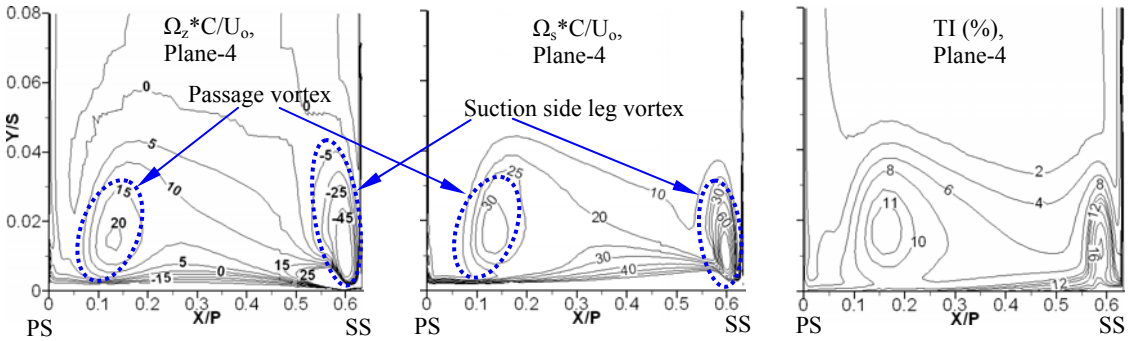

Figure 3: Computational normalized axial vorticity ($\Omega_z{*}C/U_o$), streamwise vorticity ($\Omega_s{*}C/U_o$), and overall turbulence intensity ($TI\%$) in Plane-4 at Z_G/C_{ax}=0.28.

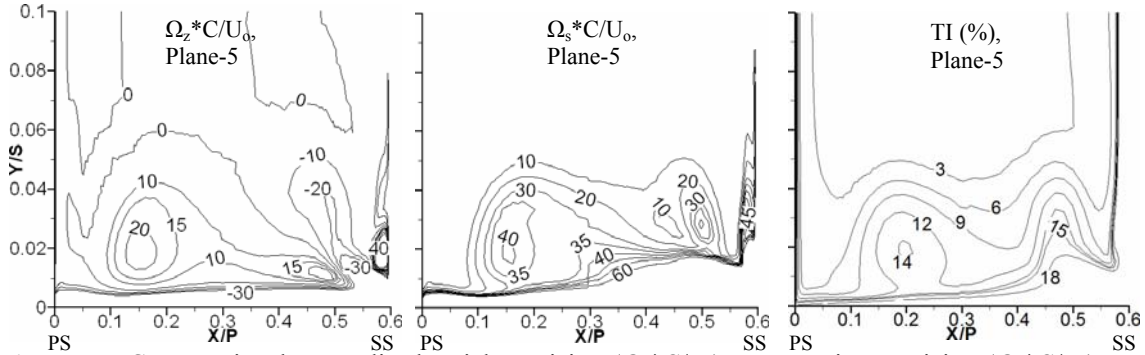

Figure 4: Computational normalized axial vorticity ($\Omega_z{*}C/U_o$), streamwise vorticity ($\Omega_s{*}C/U_o$), and overall turbulence intensity ($TI\%$) in Plane-5 at Z_G/C_{ax}=0.64.

Normalized vorticities and turbulence intensity contours in Fig. 5 show the passage vortex system as the vortex structures are transported to the suction side near the exit at Z_G/C_{ax}=0.97. The positive ($\Omega_z{*}C/U_o$)>5 contours and negative ($\Omega_z{*}C/U_o$)<-5 contours adjacent to *SS* are clearly identifiable as the passage vortex and suction side leg vortex, respectively. The centers of the vortex structures are located higher above the endwall in this plane and the suction side leg vortex is located above the passage vortex. The ($\Omega_s{*}C/U_o$) and $TI\%$ contour plots in Fig. 5 do not clearly identify the two vortex structures separately, but their high contour magnitudes adjacent to *SS* and at Y/S>0.025 indicate the passage vortex system. The high contour magnitudes above the endwall in other X/P locations are caused by the strong boundary layer turbulence. As the vortex structures lifts above the endwall, their influences on the endwall region flow are reduced.

The normalized axial wall shear stress (τ_z/P_d) and the endwall region streamlines in Fig. 6 show the locations of the vortex structures in the passage and their trajectories along endwall. The boundary layer separation near the leading edge region in Fig. 6 is indicated by τ_z/P_d ~0 contours where the horseshoe vortex, pressure side leg vortex, and suction side leg vortex are formed. The high τ_z/P_d magnitudes along the suction side in Z_G/C_{ax}<0.5 are caused by the flow accelerations in the boundary layer. The τ_z/P_d magnitudes are then low on the suction side about Z_G/C_{ax}=0.80 because of the adverse pressure gradient on the suction side. The concentration of the streamlines in Fig. 6 is very high along the flow separation line and the vortices travel along the region bounded by the separation line and boundary layer re-attachment line as shown schematically on the right hand side in Fig. 6.

The Nusselt numbers on the bottom endwall in Fig. 7 indicate the effects of the vortex structures on the heat transfer and thermal load near the leading edge region. Nusselt number is computed based on the temperature difference (T_o-T_w) and vane actual chord. Higher *Nu* in Fig7 indicates undesirable higher endwall temperature, T_w. The *Nu* are very high near the leading edge region specially along the suction side in Z_G/C_{ax}<0.5 due to the suction side leg vortex. However, the effects of the passage vortex on *Nu* are not clearly identifiable. The *Nu* increases along the endwall near the pressure side mostly due to the flow accelerations along the passage.

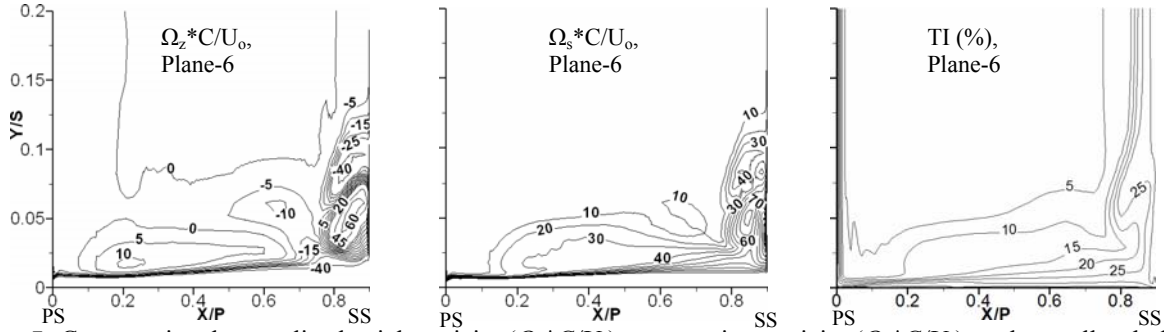

Figure 5: Computational normalized axial vorticity ($\Omega_z{*}C/U_o$), streamwise vorticity ($\Omega_s{*}C/U_o$), and overall turbulence intensity ($TI\%$) in Plane-6 at Z_G/C_{ax}=0.97.

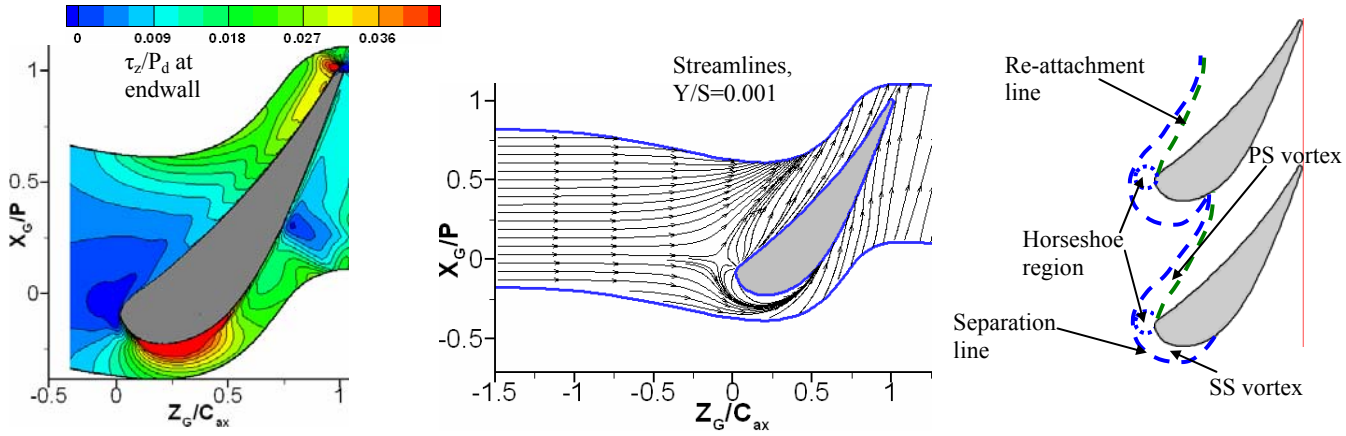

Figure 6: Computational normalized axial wall shear stress (τ_z/P_d) and near wall streamlines along bottom endwall showing boundary layer separation region and vortex flows along endwall.

(ii) Measurements: adiabatic film-cooling effectiveness

To avoid the high temperature regions on the endwall, it is necessary to protect the endwall from the hot gas streak with the film cover provided by injecting coolant through the endwall. Measurements of the adiabatic film-cooling effectiveness are obtained with the coolant holes located in the bottom wall upstream of the test section. The inlet blowing ratio (M_{in}) based on the definition provided in [11] varies between 1.0 and 2.6. The film cooling effectiveness, ε is computed from the ratio $(T_o\text{-}T_w)/(T_o\text{-}T_f)$ where T_w is the measured adiabatic wall temperature and T_f is the coolant temperature. The wall temperature is obtained from the infrared image of the measurement location through the top wall as described in [12]. As T_f/T_o is constant for the measurements, higher ε values indicate desirable lower T_w.

The effectiveness, ε along the endwall in Fig. 7 is shown for M_{in}=1.29. The cooling holes shown in the figure indicate the locations of the jets relative to the vortex structures. The ε values in Fig. 7 are higher near the suction side of the passage leaving a large endwall region along the pressure side mostly uncooled. This occurs as the coolant jets are diverted toward the suction side by the boundary layer separation region. The strong horseshoe vortex also lifts up most of the coolant jets located near the leading edge allowing small effectiveness.

Figure 8 shows the film-cooling effectiveness at higher coolant mass flux as the blowing ratio, M_{in} increases to 1.69 to 2.60. As indicated, the higher blowing ratios achieve higher ε distributions near the leading edge as well as along the pressure side endwall. The high jet momentum penetrates the boundary layer separation region to reach the pressure side endwall and thus, the ε values increase. However, the cooling effectiveness decreases near the suction side as M_{in} increases. The boundary layer fluid is energized with high momentum jets and turns less toward the suction side inside the passage. As a result, the coolant jets being carried by the boundary layer flow reach the suction side at further downstream locations with higher M_{in}.

Conclusion

The secondary flow structures along the endwall of a linear vane passage are determined numerically from their vorticity components and turbulence intensity. The flow regime employed is compressible. The computations show a passage vortex structure travels across the passage from the pressure side to suction side where it groups with a suction side leg vortex traveling along the suction side. The vortices travel very close to the endwall before they form the group and strongly influence the endwall region streamlines and heat transfer. Tests are performed

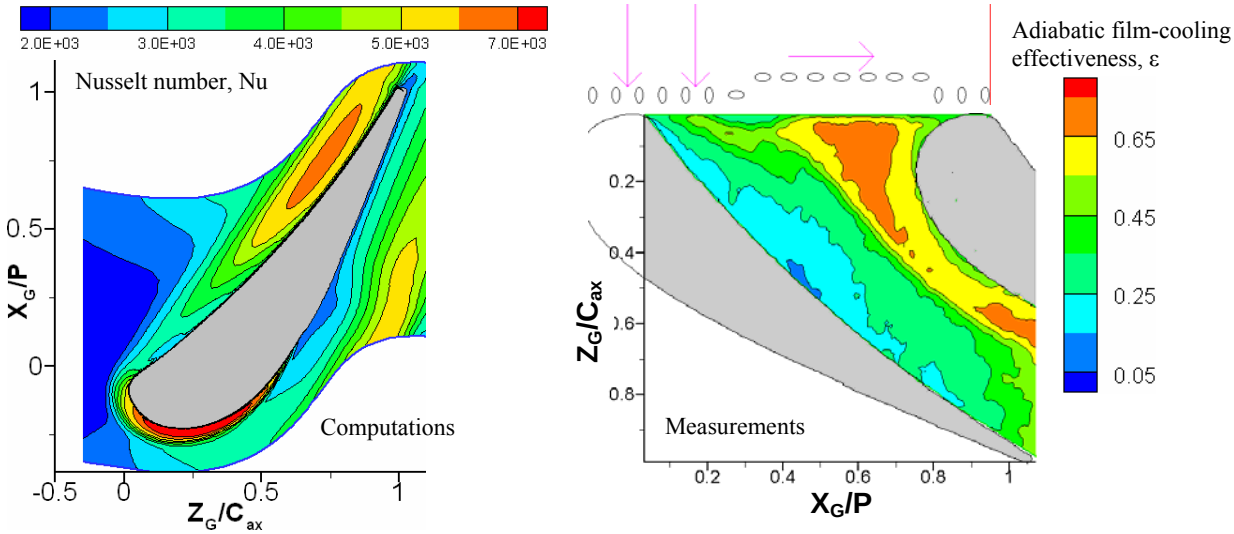

Figure 7: Distributions of computed *Nu* and measured adiabatic film-cooling effectiveness (ε) for M_{in}=1.29 along the bottom endwall.

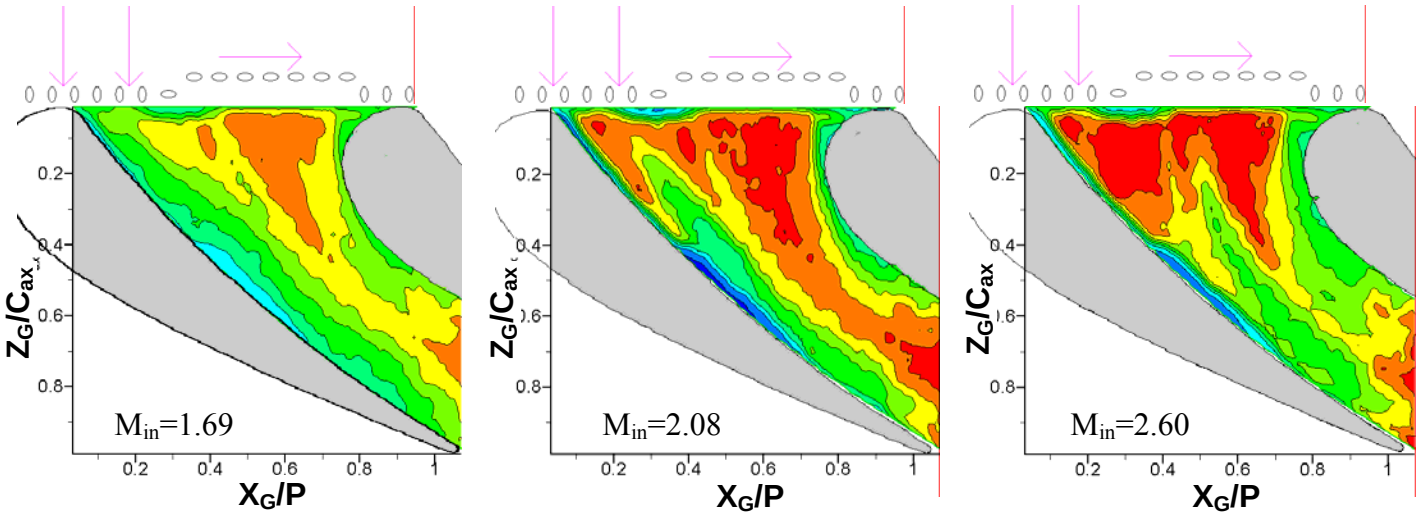

Figure 8: Measured adiabatic film-cooling effectiveness (ε) for M_{in}=1.69, 2.08, and 2.60 at T_j/T_∞=0.91 along the bottom endwall. Legends are shown in Fig. 7.

in a high speed cascade employing the same vane airfoil as in the computations and film-cooling flow injected from the endwall holes located upstream of the vane cascade. The near endwall secondary flows deflect the coolant jets re-directing and lifting them up from the endwall and significantly reduce the cooling effectiveness near the pressure side. The coolant film only reaches the pressure side endwall region and increases the cooling effectiveness when the jet momentum is increased with the blowing ratio or mass flux.

Acknowledgement

The research was supported by a grant from the US Department of Eneregy-UTSR programme. This support is gratefully acknowledged.

References

[1] Kang, M.B. and Thole, K.A., 2000, "Flow field Measurements in the Endwall region of a Stator Vane," ASME Tran. J. Turbomachinery, 122, pp. 458-466.

[2] Radomsky, R.W. and Thole, K.A., 2000, "Flow field Measurements for a Highly Turbulent Flow in a Stator Vane Passage," ASME Tran. Journal of Turbomachinery, 122 (2), pp. 255-262.

[3] Hermanson, K., Kern, S., Picker, G., and Parneix, S, 2002, "Predictions of External Heat Transfer for Turbine Vanes and Blades with Secondary Flow fields," ASME Proc. Turbo Expo, GT-2002-30206.

[4] Dominy, R.G., and Harding, S.C., 1990, "An Investigation of Secondary Flows in Nozzle Guide Vanes," AGARD Conf. Proc. No. 469, Secondary Flows in Turbomachines, pp. 7.1-7.15.

[5] Roy, R.P., Squires, K.D., Gerendas, M., Song, S., Howe, W.J., and Ansari, A., 2000, "Flow and Heat transfer at the Hub Endwall of Inlet Vane Passages- Experiments and Simulations," ASME Proc. Turbo Expo, 2000-GT-198.

[6] Thole, K.A., Knost, D.G., 2005, "Heat Transfer and Film-Cooling for the Endwall of a First Stage Turbine Vane," Int J Heat Mass Tran, 48 (25-26), pp. 5255-5269.

[7] Knost, D.G. and Thole, K.A., 2005, "Adiabatic Effectiveness Measurements of Endwall Film-Cooling for a First-Stage Vane," ASME Tran. J. Turbomachinery, 127 (2), pp. 297-305, April.

[8] Satoshi, H. and Thole, K.A., 2006, "Computational study of a midpassage gap and upstream slot on vane endwall film-cooling," ASME Proc. 51st Turbo Expo- Power for Land, Sea, and Air, Barcelona, Spain, v3 Part A, pp. 839-848, May 6-11.

[9] Barigozzi, G., Franchini, G., and Perdichizzi, A., 2006, "Endwall film cooling through fan-shaped holes with different area ratios," ASME Proc. 51st Turbo Expo- Power for Land, Sea, and Air, Barcelona, Spain, v3 Part A, pp. 599-609, May 6-11.

[10] Oke, R.A. and Simon, T.W., 2002, " Film cooling experiments with flow introduced upstream of a first stage nozzle guide vane through slots of various geometries" ASME Proc., Turbo Expo (Publication) IGTI 2002, Amsterdam, Netherlands, v3 A, pp. 33-40, June 3-6.

[11] Gustafson, R., Mahmood, G.I., and Acharya, S., 2007, "Flow Field in a Film-Cooled Three-Dimensional Contoured Endwall Passage: Aerodynamic Measurements", ASME Proc. Turbo Expo 2007, Montreal, Canada, May 14-16, GT2007-28154.

[12] Mahmood, G.I., Gustafson, R., and Acharya, S., 2005, "Experimental Investigation of Flow Structure and Nusselt Number in a Low Speed Linear Blade Passage With and Without Leading Edge Fillets", ASME Trans. J. Heat Transfer, Vol. 127, pp. 499-512.